Pulsed Plasma-Chemical Synthesis of Cu_xO_y-TiO_2 Nanocomposite

G. Kholodnaya*, D. Ponomarev, R. Sazonov and O. Lapteva

Tomsk Polytechnic University, 2a Lenin Avenue, Tomsk 634028, Russia

(Received 6 May 2022, Accepted 30 June 2022)

The Cu_xO_y-TiO_2 nanocomposite was synthesized by a pulsed plasma-chemical method. Pulsed plasma-chemical synthesis was performed using a laboratory bench, which included a TEA-500 pulsed electron accelerator and a reaction chamber. The structure of the composite was studied by X-ray phase analysis and transmission electron microscopy. The dependence of the geometric mean size, morphology, and phase composition of the composite on the molar ratio of reagents in the initial mixture, such as a reaction chamber, was confirmed. The morphology of the particles of the Cu_xO_y-TiO_2 nanocomposite with the core/shell structure changed into spherical particles with a uniform porous structure. The phase composition with a predominant rutile phase transformed to a mixture of several crystalline phases (anatase, rutile, copper chloride).

INTRODUCTION

A large number of studies have focused on the photocatalytic activity of titanium dioxide (TiO_2) nanopowders, as evidenced by more than 80 papers published from January to April 2021 in Scopus [1-4]. This is due to the potential use of titanium dioxide-based photocatalysts in wastewater and air purification, self-cleaning glasses to be used in buildings and automotive equipment, and the treatment of the surface of walls in hospitals and public buildings to reduce the level of bacterial contamination [5-14]. However, due to the peculiarities of the band structure of TiO_2, this material exhibits its photocatalytic properties only when exposed to electromagnetic radiation in the UV range, which means that it can use only about 4% of the intensity of sunlight radiation [5-7]. For this reason, the development of materials based on titanium dioxide with more efficient use of the visible range of electromagnetic radiation is of great importance. There are several ways to increase the photocatalytic activity of titanium dioxide,

including the following: 1) the synthesis of TiO_2 nanostructures of a given phase composition and morphology and 2) the production of composite materials with metal and semiconductor nanoparticles. The preparation of nanocomposites based on titanium dioxide and copper(II) oxide (CuO) is done based on the fact that CuO, as a dopant, affects the phase composition of TiO_2. It has been shown that in CuO-TiO_2 systems, the change in the anatase/rutile phase ratio is dependent on the CuO concentration [10-13], which, in turn, changes the photocatalytic properties of the prepared nanocomposites.

The influence of the CuO content (0-15 wt.%) in the CuO-TiO_2 composite on its photocatalytic properties was studied [10]. It was found that 1.25 wt.% of the CuO content in the composite was the optimal content for the production of H_2 from a mixture of ethanol and water under UV exposure. In another study [11], CuO_x-TiO_2 nanocomposite was prepared by the impregnation method. This study demonstrated how the copper content (0.1 to 2 wt.%) and calcination temperature (200, 300, 400, and 500 °C) affected the photocatalytic activity of the CuO_x-TiO_2 nanocomposite. The optimum copper content and calcination temperature

*Corresponding author. E-mail: galina_holodnaya@mail.ru

were 2 wt.% and 300 °C, respectively.

CuO-TiO$_2$ composites in the form of nanorods with a core-shell structure were synthesized by the sol-gel method [11]. The synthesized CuO-TiO$_2$ composites of nanorods with a core-shell structure had a high specific capacity (400 mAhg^{-1} at 0.1 C rate) and cycle stability (94% after 100 cycles). A CuO-TiO$_2$ composite was prepared by the hydrothermal method [13]. In the CuO-TiO$_2$ nanocomposite, the production of H$_2$ was 15 times higher than that of TiO$_2$ and 16 times higher than that of pure CuO.

A CuO-TiO$_2$ nanocomposite was prepared by electrochemical oxidation [15]. The composite was tested as a catalyst in the electrocatalytic reduction of NH$_3$. In another study, a CuO-TiO$_2$ composite with a core-shell structure was synthesized from Cu(NO$_3$)$_2$·3H$_2$O and tetrabutyl orthotitanate (TBOT) by a chemical method [16]. Based on the results, it was offered that the CuO-TiO$_2$ composite could be used in the manufacture of high-performance dielectrics in electrical appliances. The use of a CuO-TiO$_2$ composite as a sensor was investigated in [17]. The optical, chemical, and electrical properties of the CuO-TiO$_2$ composite were studied in [18]. Due to the narrow band gap of CuO nanoclusters (about 1.7 eV), the composite showed high photocatalytic activity in visible light. In addition, CuO-TiO$_2$ nanocomposites have been used as a catalyst, a gas sensor, a glucose level sensor, and an element in lithium-ion batteries [19-26].

In the present work, electrospark and pulsed plasma-chemical methods were used to synthesize Cu$_x$O$_y$-TiO$_2$ nanocomposites. The aim of this work was to study the phase and chemical composition and morphology of the Cu$_x$O$_y$-TiO$_2$ nanocomposites based on the concentration of the initial reagents and the design of the reaction chamber.

EXPERIMENTAL

Materials

To prepare Cu$_x$O$_y$ samples, a copper plate (98.6%) was used. TiO$_2$ was synthesized using titanium tetrachloride (TiCl$_4$, 99.9%), oxygen (O$_2$, 99.9%), and hydrogen (H$_2$, 99.9%). The initial reagents were purchased from Sigma-Aldrich and used without any further purification.

Synthesis of Cu$_x$O$_y$ Nanoparticles

The Cu$_x$O$_y$ particles were synthesized by the electrospark method [27-28]. A laboratory stand was used, which included an electrode system, a movement system, a system for measuring processing parameters (an oscilloscope and a current sensor, a high voltage divider, and a pressure gauge), a source of current pulses, and a vacuum system (a vacuum pump, gas cylinders with a working gas, gas routes, and gas taps). More specifically, the laboratory stand used a power supply circuit consisting of two generators operating at one interelectrode gap. The generator consisted of three main units as follows: a low-voltage part, a high-voltage part, and a control system. The high-voltage part of the generator is designed to form the initial spark channel. The low-voltage part of the generator is used to transfer the energy of the capacitor to the spark channel. The main parameters of the generator were as follows: a) a high-voltage part: pulse duration was 1 μs, pulse amplitude was 18 kV, and pulse energy was 0.01 J; b) a low-voltage part: pulse duration was 5-100 μs, the stored energy was 0.1-0.6 J, and the pulse repetition rate was 0.1-5 kHz. The electrode system was located inside a vacuum cell and consisted of two electrodes, of which one was stationary and made in the form of a pointed rod (tip) and the other one was a metal table of the movement system (plane). Both electrodes were isolated from the other parts of the setup, which allowed the polarity of the electrodes to be changed. A coordinate table with two degrees of freedom and an insulated table was used as a sample movement system. The coordinate table was moved by two stepper motors, providing a positioning accuracy of 2.5 microns. The size of the processing area was 150 mm × 250 mm. The stepper motors were controlled by the plant control system. To ensure the pumping of air to a pressure of 10^{-2} Torr, an NVR-5D rotary vane pump was used. Figure 1 shows a schematic diagram of the experiment on the synthesis of nanosized Cu$_x$O$_y$.

The electrospark method for producing nanoparticles can be described as follows: a copper plate is located in the chamber, which is an electrode. After preliminary evacuation, the gas cell is filled with gas (argon). At the end of this stage, the pulse generator starts up. At the same time, the system for moving the copper plate is automatically
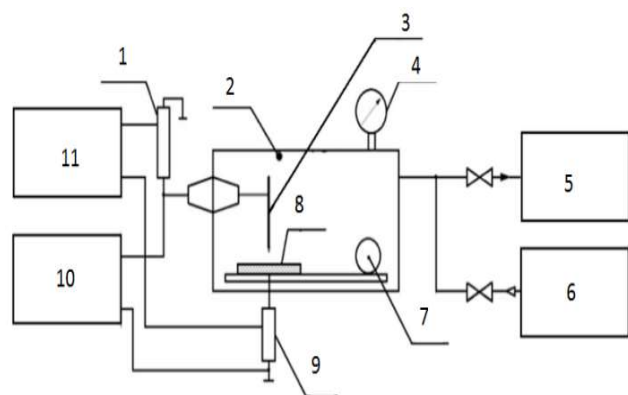
Fig. 1. The experimental scheme of the synthesis of nanosized Cu$_x$O$_y$: 1- HV divider, 2- cuvette, 3- HV electrode, 4- manovacuum meter, 5- vacuum pump, 6- gas vessel, 7- mobility system, 8- copper plate, 9- current sensor, 10- pulse generator, 11- oscillograph.

turned on and the process of producing nanoparticles begins. Upon completion of this process, the generator turns off automatically and the travel system returns to the starting point. The method for producing nanoparticles is based on the use of the energy of an electric spark discharge formed between the electrode and the target. When a voltage pulse is applied between the electrode and the target surface, a spark breakdown plasma channel with an initial diameter of ~ 0.1 mm is formed. The current passing through the channel heats it up, the pressure in the channel rises, and the channel expands. The plasma temperature reaches values of 3.8×10^4 K while the energy flux density is 10^6-10^9 J m^{-2}. As a result of the action of a concentrated energy flux on the target, a rapid local overheating of the surface is formed, leading to the sublimation of the material. Under the influence of gas-dynamic forces, the target material is removed from the discharge area, where it is condensed and a nanopowder is formed, and due to the special design of the electrode system, the as-prepared nanoparticles settle in a special trap.

Synthesis of Cu$_x$O$_y$-TiO$_2$ Nanocomposites

The Cu$_x$O$_y$-TiO$_2$ nanocomposites were synthesized using an experimental stand, which included a TEA-500 pulsed electron accelerator (Tomsk, Russia) and a reaction chamber

[30]. The TEA-500 pulsed electron accelerator consisted of the following main units: a gas-filled pulse voltage generator (assembled according to the Arkady-Marx scheme), a double forming line, an autotransformer, and a diode unit. The presence of an autotransformer in the accelerator was its special feature. An autotransformer was used to match a low-resistance double-forming water line with a high-resistance impedance of an explosive-emission planar diode during the formation of a working pulse. The electron beam in the TEA-500 accelerator was formed due to the field emission from the surface of a graphite cathode with a diameter of 45 mm. The electron beam was extracted through an anode window, which was a supporting grid (with an optical transparency of 95%) and an aluminum foil of 140 μm thick. The anode-cathode gap for all experiments was 13 mm. The accelerator was equipped with the necessary diagnostic tools for beam parameters, including particle energy, current and current density, and total energy transferred by the beam. The stability of the accelerator was constantly monitored. The main parameters of the accelerator were as follows: 420 keV electron energy, up to 7 kA current supplied to the diode unit, 60 ns half-amplitude pulse duration, 1-5 pps repetition rate, and up to 200 J pulse energy.

In this research, two types of reaction chambers (diameter: 15.1 cm, length: 32 cm) were: quartz and copper. The reaction chambers were equipped with pressure sensors and shut-off and control valves for the inlet of the initial reagent mixture and gas pumping. Before admitting the gas mixture, the reaction chamber was evacuated to a pressure of ~ 3-5 Torr, and an electron beam was injected from the end of the reaction chamber. Figure 2 shows a diagram of the experimental setup.

The Cu$_x$O$_y$-TiO$_2$ nanocomposite was synthesized in the reaction chamber using a nanosecond electron beam to generate a low-temperature plasma from a gas-phase mixture (*i.e.*, TiCl$_4$, O$_2$, and H$_2$). The volumetric excitation of the reaction gas by a pulsed electron beam occurred, and the reactions proceeded in the entire volume of the reaction chamber. A pulsed electron beam initiated a complex of chemical reactions, including chain reactions (*i.e.*, the oxidation of hydrogen and the combination of chlorine with hydrogen). The energy consumption of the beam was significantly lower than the energy of chemical endothermic
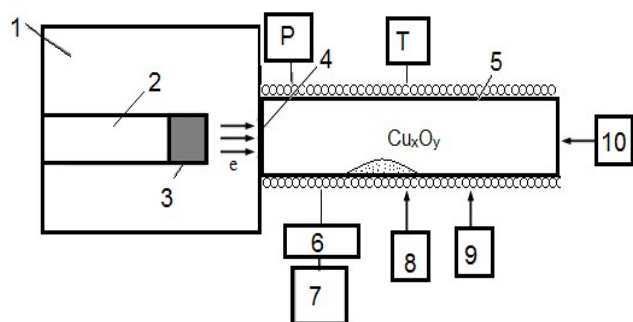
Fig. 2. The experimental stand: 1- TEA-500 diode chamber, 2- cathode holder, 3- cathode (graphite, diameter = 45 mm), 4- anode grid (3 mm thick) and aluminum foil (140 μm thick), 5- reaction chamber, 6- product collection system, 7- vacuum pump, 8- H_2 cylinder, 9- O_2 cylinder, and 10- $TiCl_4$ dispenser.

fusion reactions. The energy balance of the process was ensured by the exothermic reactions of oxidation and chlorination of hydrogen. The synthesis of the Cu_xO_y-TiO_2 nanocomposite occurred in one pulse of an electron beam. After the injection of an electron beam into the mixture, the nanopowder was formed in the reaction chamber. Nanocomposites with high chemical purity were prepared by the pulsed plasma-chemical method due to the absence of the possibility of technological contaminants at high temperatures. In a series of experiments within the framework of this study, the reaction chamber was heated to a temperature of 70 °C for the transition of liquid $TiCl_4$ to the gaseous state. The concentrations of the initial reagents are presented in Table 1.

Characterization of Cu_xO_y-TiO_2 Nanoparticles

To determine the morphology of Cu_xO_y-TiO_2

nanocomposites, a JEOL-II-100 transmission electron microscope with an accelerating voltage of 200 kV (JEOL, Japan) was used.

To determine the crystal structure of the nanocomposite system, a standard X-ray phase analysis technique was used. The reaction products were analyzed using a Shimadzu XRD-6000/7000 diffractometer (Shimadzu, Japan).

The sizes of coherent scattering regions (CSR) of crystalline Cu_xO_y-TiO_2 nanocomposites were calculated using the Scherrer equation [31-32]: $d = K\lambda/\beta cos\theta$, where K is a constant, whose value varies from 0.62 to 2.08 and characterizes the shape and distribution by the size of crystallites (in this study, K = 0.9 was used in the approximation of the spherical shape of crystallites), λ is the radiation wavelength of CuKα (0.1542 nm), β is the peak width at half maximum (rad), and θ is its position.

RESULTS AND DISCUSSION

Figures 3-6 present the typical TEM images of Cu_xO_y-TiO_2 nanocomposites. Figure 3 shows that the Cu_xO_y-TiO_2 nanocomposite had a core/shell structure. The nuclei had a shape close to spherical; however, the nuclei of an oval shape can also be distinguished. The average geometric size of the Cu_xO_y-TiO_2 nanocomposite did not exceed 250 nm. All particles were covered with a shell, the thickness of which did not exceed 40 nm. Moreover, some of the particles were covered with a dense adjoining shell (Fig. 3a), and for some of the particles, a distance was observed between the core and the shell (Fig. 3b). Sample 1 of the Cu_xO_y-TiO_2 nanocomposite was characterized by weak particle agglomeration.

The morphology of particles of sample 2 of the synthesized Cu_xO_y-TiO_2 nanocomposite was represented by

Table 1. The Concentration of Initial Reagents

S. No.	Type of reaction chamber	$TiCl_4$ (mmol)	H_2 (mmol)	O_2 (mmol)	Cu_xO_y (g)
1	Quartz	32	26	80	0.4
2	Quartz	36	26	100	0.4
3	Quartz	50	26	130	0.4
4	Copper	36	26	100	0.4
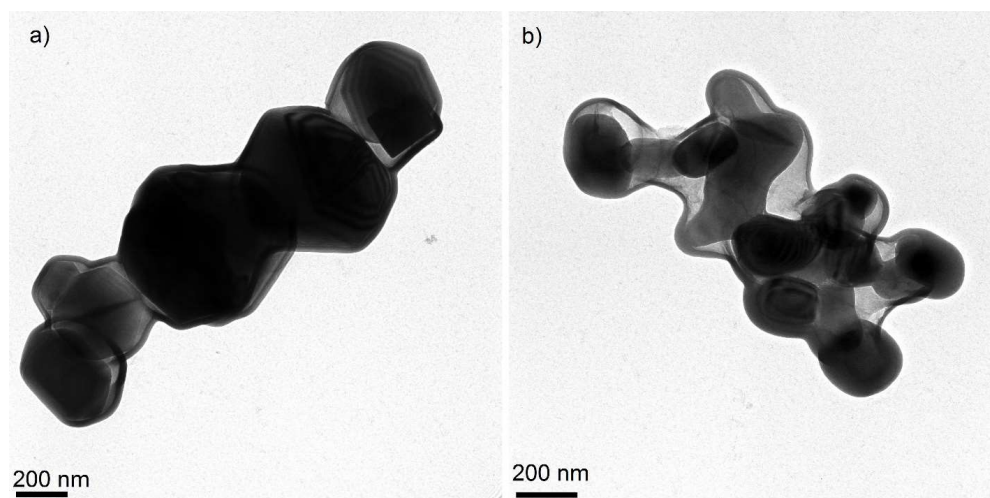
Fig. 3. The TEM images of Cu_xO_y-TiO_2 (sample 1).
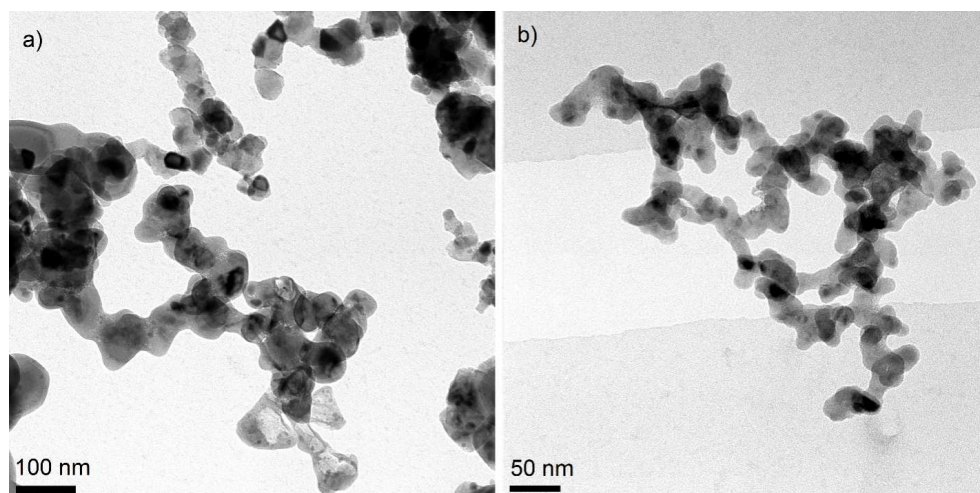
Fig. 4. The TEM images of Cu_xO_y-TiO_2 (sample 2).
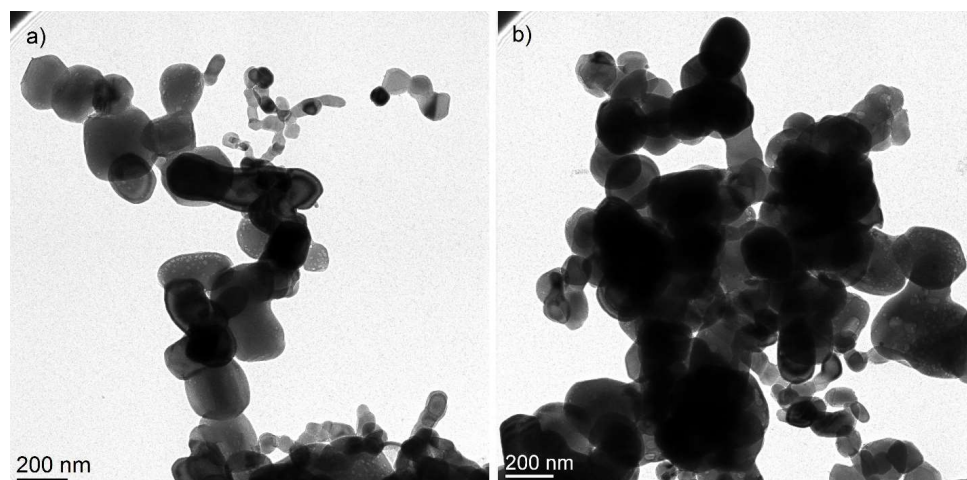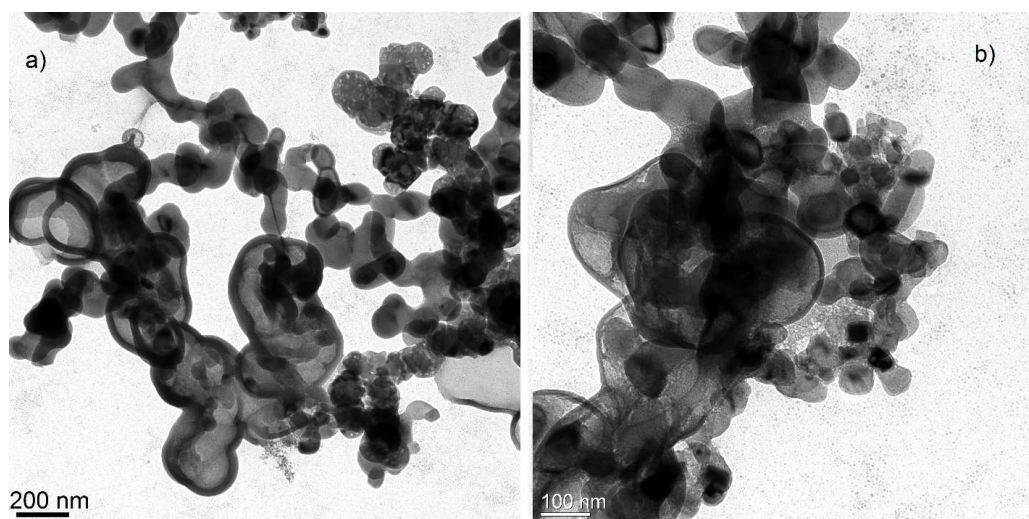

Fig. 5. The TEM images of Cu_xO_y-TiO_2 (sample 3).

429

Fig. 6. The TEM images of Cu_xO_y-TiO_2 (sample 4).

particles of irregular shape with smoothed edges and oval shape (Fig. 4). The average geometric particle size was 50-70 nm, and the particles were highly agglomerated. Some smaller particles were found on the surface of some of the synthesized particles. The size of these smaller particles did not exceed 5-7 nm.

With an increase in the concentration of $TiCl_4$ and O_2 in the initial mixture of reagents, the morphology of the synthesized Cu_xO_y-TiO_2 nanocomposite changed. There were large spherical particles with a uniform porous structure (Fig. 5a). The average geometric particle size was 150-200 nm, and the pore size did not exceed 30 nm. The sample contained a fine fraction of oval-shaped particles, and the average particle size of the fine fraction was 40-80 nm. The particles of the synthesized Cu_xO_y-TiO_2 nanocomposite combined with each other to form agglomerates (Fig. 5b).

The morphology of sample 4 of the Cu_xO_y-TiO_2 nanocomposite synthesized in a copper reaction chamber was represented by three different types of particle. The first type of particle was spherical, with a uniform porous structure (with an average geometric size of 80-120 nm). The second type of particle had a core/shell structure. Here, the size of the cores did not exceed 40-60 nm, the shell thickness was 10-15 nm, and the distance from the shell to the core reached 90 nm. The third type of particle had the shape of polygons or a shape close to spherical (with an average geometric particle size of 50 nm). Sample 4 was characterized by

particle agglomeration.

The mechanism of the formation of the porous structure of the Cu_xO_y-TiO_2 nanocomposite, as illustrated in Figs. 5-6, can be explained by the formation of titanium dichloride oxide during the pulsed plasma-chemical synthesis. Titanium dichloroxide was formed by the action of chlorine on titanium oxide.

$$TiO + Cl_2 \rightarrow TiOCl_2 \tag{1}$$

In addition, the action of oxygen on titanium tetrachloride due to the plasma in the reaction chamber led to the formation of titanium dichloride oxide. Moreover, titanium dichloride oxide was also formed by the action of chlorine oxide on titanium tetrachloride:

$$TiCl_4 + Cl_2O \rightarrow TiOCl_2 + 2Cl_2 \tag{2}$$
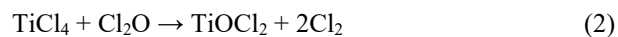
When the vapors of titanium tetrachloride over titanium dioxide passed a certain amount, the following compound was formed:

$$TiCl_4 + TiO_2 \rightarrow TiOCl_2 \tag{3}$$

Due to these reactions, titanium dichloride was always present in a certain amount in the products of hydrolysis of titanium tetrachloride with water vapor and in the products of oxidation of titanium tri- and dichloride with oxygen.

Thus, a film consisting not only of titanium oxide but also of titanium oxychloride grew on the surface of Cu_xO_y particles. In this case, gas evolution in the reactions of TiO_2 synthesis occurred both from the surface of the film to the outside and to the inside of the shell, which, in turn, resulted in the "inflation" of the shell.

Under the action of an electron beam on titanium tetrachloride, the Ti-Cl covalent bond broke and atomic chlorine was formed, which, in turn, reacted with the metallic part of copper in Cu_xO_y nanoparticles, leading to the formation of $CuCl_2$ and the release of a significant amount of heat by the reaction:

$$Cu + Cl_2 \rightarrow CuCl_2 + Q \qquad (4)$$

Titanium oxychloride in the shell decomposed when heated according to the following reaction:

$$TiOCl_2 \ (T) \rightarrow TiO_2 + TiCl_4 \qquad (5)$$
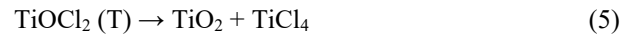
It can be assumed that the shell layer of the Cu_xO_y-TiO_2 nanocomposite was opened and pores were formed on its surface. Figure 7 shows the microdiffraction patterns of samples 1 and 4 of the Cu_xO_y-TiO_2 nanocomposite. The microdiffraction patterns contained bright, well-defined structural reflections, which indicated the presence of crystalline phases of anatase and rutile, which was confirmed by XRD analysis (Fig. 8).
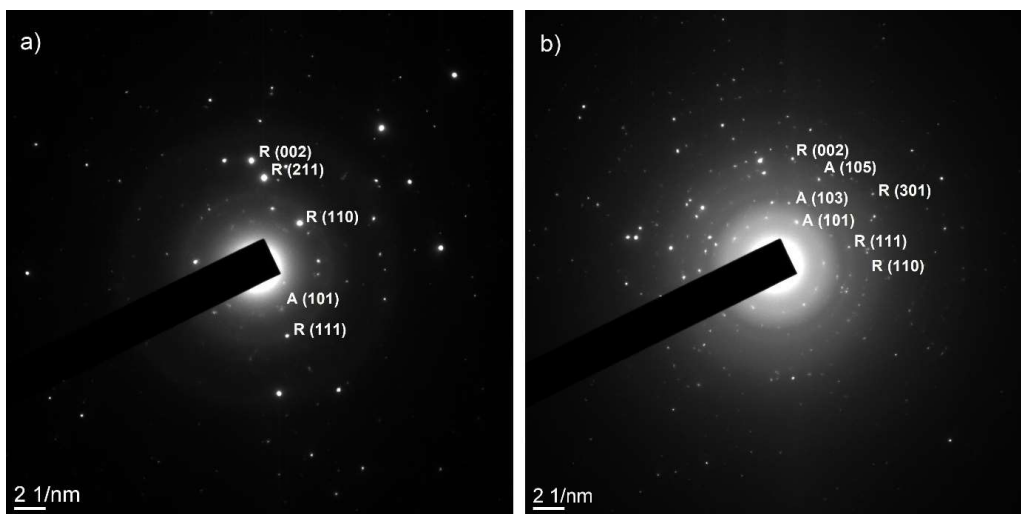

Fig. 7. Microdiffraction patterns of samples 1 (a) and 4 (b) of the Cu_xO_y-TiO_2 nanocomposite.

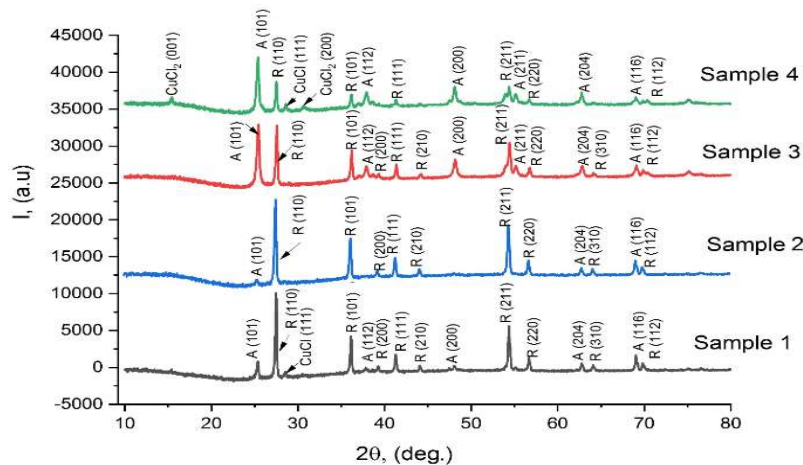**Fig. 8.** The XRD pattern of the Cu_xO_y-TiO_2 nanocomposite (A- anatase and R- rutile).

It can be seen from the analysis of the obtained XRD data that the crystal lattices of anatase and rutile were stably formed in all samples (JCPDS Card no. 00-021-1272, JCPDS Card no. 00-021-1276). For samples 1-3, a low-intensity peak was recorded, which, according to JCPDS Card no. 33-0451, can be attributed to $CuCl_2 \cdot 2H_2O$ (221). For samples 1 and 4, a small peak ($2\theta = 28.56°$) corresponded to the crystalline phase CuCl (111) (JCPDS Card no. 00-006-0344). The X-ray diffraction pattern of sample 4 showed low-intensity peaks ($2\theta = 15.36°$ and $30.64°$), which are characteristic of the crystalline phase of $CuCl_2$ (JCPDS Card no. 35-0690). Moreover, the content of crystalline phases in Cu_xO_y-TiO_2 nanoparticles was calculated (Table 2). The diffraction of synthesized Cu_xO_y-TiO_2 composites enabled us to determine the CSR using the Debye-Scherrer equation (Table 3).

Changes in the concentration of the initial reagents and the type of the reaction chamber did not affect the CSR size of the synthesized Cu_xO_y-TiO_2 nanocomposites. However, some changes were observed in the content of anatase and rutile in the synthesized samples. With an increase in the oxygen concentration in the mixture of initial reagents, the anatase content in the synthesized nanocomposites increased. Furthermore, the nanocomposite synthesized in a copper reaction chamber contained more anatase than the sample produced in a quartz reaction chamber. As is known, the process temperature affects the formation of crystalline phases. Pulsed plasma-chemical synthesis proceeds with different energy release rates depending on the type of the reaction chamber and the oxygen concentration in the initial mixture of reagents, which together influence the type of the formed crystal lattice in the final synthesis product.

The synthesized Cu_xO_y-TiO_2 nanocomposites were studied using energy-dispersive X-ray spectroscopy (EDX method), in which the synthesized samples were deposited on a carbon replica located on a copper lattice. Color windows displaying sample elements are shown in Fig. 9. Based on the comparison of the elements Cu, Ti, and O shown in **Fig. 10,** it can be assumed that the chemical elements Cu, Ti, and O were uniformly distributed in the synthesized Cu_xO_y-TiO_2 nanocomposites.

Table 2. The Content of Crystalline Phases in Cu_xO_y-TiO_2 Nanoparticles

S. No.	A (%)	R (%)	CuCl (%)	CuCl₂ (%)
1	15.9	80	4.1	-
2	13.9	86.1	-	-
3	48.1	51.9	-	-
4	72.5	13.9	7.1	6.5

Table 3. The CSR of Cu_xO_y-TiO_2 Nanoparticles

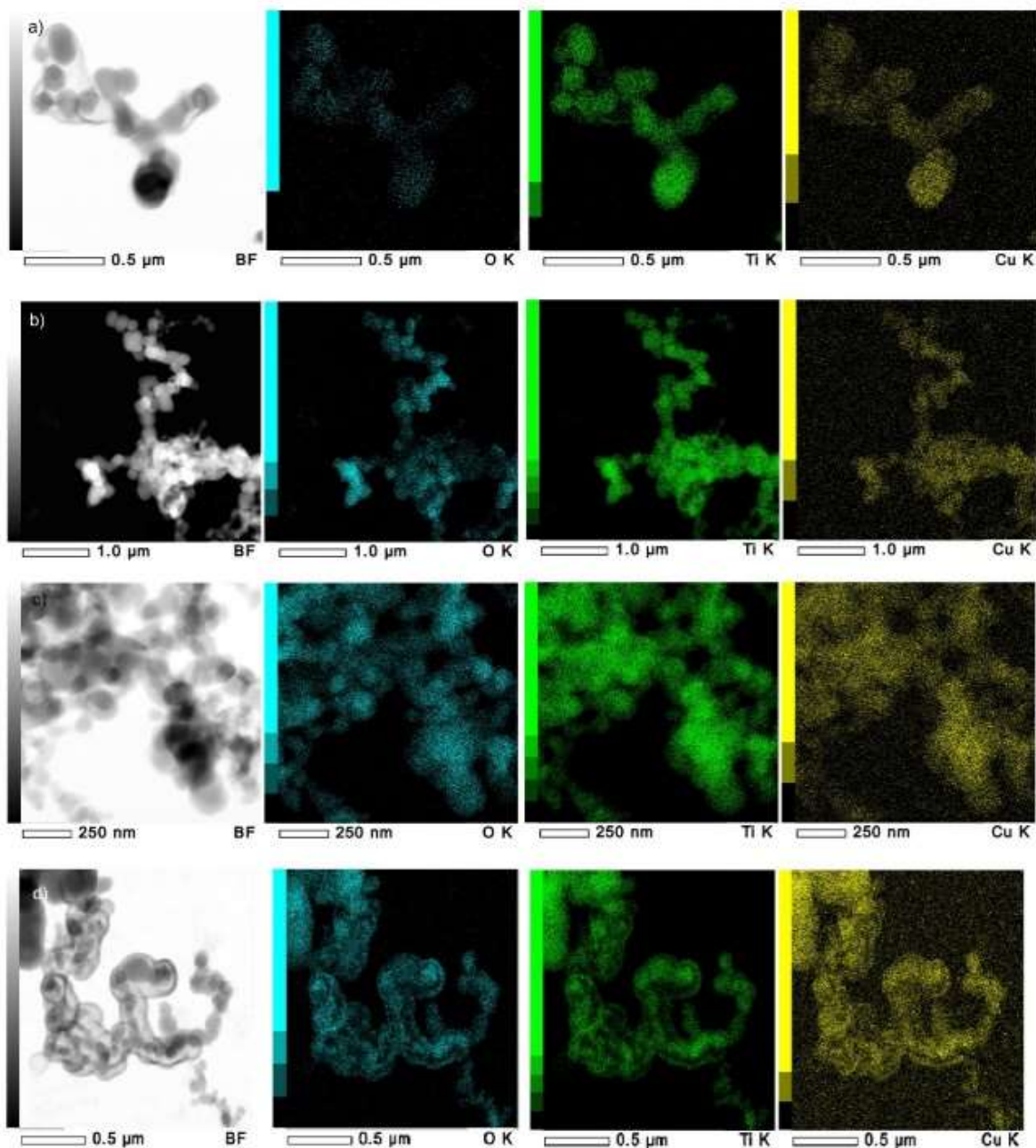| S. No.	Diffraction angle (2θ)	Atomic planes (h k l)	Crystalline phase	CSR (nm)
1	25.281	(1 0 1)	A	33
	27.446	(1 1 0)	R	41
2	-	-	-	-
	27.446	(1 1 0)	R	44
3	25.281	(1 0 1)	A	32
	27.446	(1 1 0)	R	41
4	25.281	(1 0 1)	A	29
	27.446	(1 1 0)	R	37

Fig. 9. The color windows reflect the elements of samples 1 (a), 2 (b), 3 (c), and 4 (d) of Cu_xO_y-TiO_2 nanocomposite.

CONCLUSIONS

In this work, Cu_xO_y-TiO_2 nanocomposites were prepared using a pulsed plasma-chemical method. Studies of the main physicochemical properties (*i.e.*, morphology and phase composition) of Cu_xO_y-TiO_2 nanocomposites showed that the pulsed plasma-chemical method can be used to synthesize Cu_xO_y-TiO_2 nanocomposites with predetermined properties by changing the concentration of initial reagents or the type of a reaction chamber. When the content of oxygen and titanium tetrachloride was increased in the initial mixture, some particles with complex morphology were formed and

the geometric size of the synthesized particles decreased. Some changes were also observed in the phase composition. Using a copper reaction chamber, a nanocomposite with complex particle morphology and several crystalline phases was prepared. Thus, it can be stated that the concentration of the initial reagents determined the amount of energy during the oxidation and chlorination of hydrogen. As a result, there was a change in the local temperature of the process, which played a decisive role in the formation of the composite. In addition, during the implementation of the pulsed plasma-chemical synthesis, the material on the walls of the reaction chamber entered into chemical interaction with the vapor of wet hydrogen chloride to form $CuCl_2$. Finally, the efficiency of the process initiation was determined by the process of dissipation of the energy of a pulsed electron beam, which depends on the conductivity of the chamber walls [33].

ACKNOWLEDGMENTS

REFERENCES

[1]   da Silva, É. F. M.; Ximenes, É. R. B.; de Sales, L. B. V.; Dantas, E. J. M.; Oliveira, E. D. C.; Simões, T. B.; Ribeiro, A. T. S.; Sanz, O.; Machado, G.; Almeida, L. C., Photocatalytic Degradation of RB5 Textile Dye Using Immobilized TiO_2 in Brass Structured Systems. *Catal. Today.* **2022**, *383*, 173-182, DOI: 10.1016/j.cattod.2021.02.006.

[2]   Yoo, H.; Hyeun Kim, J., Photoactive TiO_2/CuxO Composite Films for Photocatalytic Degradation of Methylene Blue Pollutant Molecules. *Adv. Powder. Technol.* **2021**, *32*(4), 1287-1293, DOI: 10.1016/j.apt.2021.02.031.

[3]   Srevarit, W.; Moonmangmee, S.; Phapugrangkul, P.; Kuboon, S.; Klamchuen, A.; Saito, N.; Ponchio, C., Photoelectrocatalytic H_2 Evolution Enhancement Over CuO-decorated TiO_2 Nanocatalysts and Promoting E. coli degradation. *J. Alloys. Compd.* **2021**, *859*, 157818,

[4]   Zhang, J.; Tian, H.; Yu, Y.; Jiang, Z.; Ma, M.; He, C., Novel $CuO@TiO_2$ Core-Shell Nanostructure Catalyst for Selective Catalytic Reduction of NOx with NH_3. *Catal. Lett.* **2021**, *151*(9), 2502-2512, DOI: 10.1007/s10562-020-03515-2.

[5]   Snider, G.; Ariya, P., Photo-catalytic Oxidation Reaction of Gaseous Mercury over Titanium Dioxide Nanoparticle Surfaces. *Chem. Phys. Lett.* **2010**, *491*(1-3), 23-28, DOI: 10.1016/j.cplett.2010.03.062.

[6]   Qian, X.; Yang, W.; Gao, S.; Xiao, J.; Basu, S.; Yoshimura, A.; Shi, Y.; Meunier, V.; Li, Q., Highly Selective, Defect-Induced Photocatalytic CO_2 Reduction to Acetaldehyde by the Nb-Doped TiO_2 Nanotube Array under Simulated Solar Illumination. *ACS Appl. Mater. Interfaces.* **2020**, *12*(50), 55982-55993, DOI: 10.1021/acsami.0c17174.

[7]   Wei, Z.; Chen, S.; Fang, Y.; Wang, Z.; Liang, K.; Amakanjaha, A.C.; Zhong, Y., How Anatase TiO_2 with {101} {001} and {100} Surfaces Affect the Photooxidation Process of Roxithromycin. *Water Sci. Technol.* **2020**, *82*(12), 2877-2888, DOI: 10.2166/wst.2020.538.

[8]   Li, F.; Chen, X.; Guo, Q.; Yang X., Hydrogen Production via Methanol Photocatalysis on Au/Rutile-TiO_2(110). *J. Phys. Chem. B.* **2020**, *124*(49), 26965-26972, DOI: 10.1021/acs.jpcc.0c09520.

[9]   Fang, S.; Liu, Y.; Sun, Z.; Lang, J.; Bao, C.; Hu, Y. H., Photocatalytic Hydrogen Production over Rh-loaded TiO_2: What is the Origin of Hydrogen and How to Achieve Hydrogen Production from Water? *Appl. Catal. B.* **2020**, *278*, 119316, DOI: 10.1016/j.apcatb.2020.119316.

[10] Chen, W. -T.; Jovic, V.; Sun-Waterhouse, D.; Idriss, H.; Waterhouse, G. I. N.; The Role of CuO in Promoting Photocatalytic Hydrogen Production over TiO_2. *Int. J. Hydrogen Energy.* **2013**, *38*(35), 15036-15048, DOI: 10.1016/j.ijhydene.2013.09.101.

[11] Jung, M.; Scott, J.; Ng, Y. H.; Jiang, Y.; Amal, R., CuOx Dispersion and Reducibility on TiO_2 and its Impact on Photocatalytic Hydrogen Evolution. *Int. J. Hydrogen Energy.* **2014**, *39*(24), 12499-12506, DOI: 10.1016/j.ijhydene.2014.06.020.

[12] Chen, C.; Lee, S. H.; Cho, M.; Lee, Y., Core-shell

CuO@TiO$_2$ Nanorods as a Highly Stable Anode Material for Lithium-ion Batteries. *Mater. Lett.* **2015**, *140*, 111-114, DOI: 10.1016/j.matlet.2014.10.138.

[13] Manjunath, K.; Souza, V. S.; Ramakrishnappa, T.; Nagaraju, G.; Scholten, J. D.; Dupont, J., Heterojunction CuO-TiO$_2$ Nanocomposite Synthesis for Significant Photocatalytic Hydrogen Production. *Mater. Res. Express.* **2016**, *3*(11), 115904, DOI: 10.1088/2053-1591/3/11/115904.

[14] He, X.; Zhang, G.; Wang, X.; Hang, R.; Huang, X.; Qin, L.; Tang, B.; Zhang, X., Biocompatibility, Corrosion Resistance and Antibacterial Activity of TiO$_2$/CuO Coating on Titanium. *Ceram. Int.* **2017**, *43*(18), 16185-16195, DOI: 10.1016/j.ceramint.2017.08.196.

[15] Adamu, H.; McCue, A. J.; Taylor, R. S. F.; Manyar, H. G.; Anderson, J. A.; Simultaneous Photocatalytic Removal of Nitrate and Oxalic Acid over Cu$_2$O/TiO$_2$ and Cu$_2$O/TiO$_2$-AC composites. *Appl. Catal. B.* **2017**, *217*, 181-191, DOI: 10.1016/j.apcatb.2017.05.091.

[16] Wang, X.; Li, Y.; Li, Z.; Zhang, S.; Deng, X.; Zhao, G.; Xu, X., Highly Sensitive and Low Working Temperature Detection of Trace Triethylamine based on TiO$_2$ Nanoparticles Decorated CuO Nanosheets Sensors Sens. *Actuators. B. Chem.* **2019**, *301*, 127019, DOI: 10.1016/j.snb.2019.127019.

[17] Farah, J.; Ibadurrohman, M.; Slamet, Synthesis of CuO-TiO$_2$ Nano-composite for Formaldehyde Degradation application. AIP Conference Proceedings "5th International Symposium on Applied Chemistry 2019", Tangerang; Indonesia; 23 October 2019 - 24 October **2019**; Code 154835, *2175*, 020044, DOI: 10.1063/1.5134608.

[18] Bahadori, E.; Ramis, G.; Zanardo, D.; Menegazzo, F.; Signoretto, M.; Gazzoli, D.; Pietrogiacomi, D.; Di Michele, A.; Rossetti, I., Photoreforming of Glucose over CuO/TiO$_2$. *Catalysts.* **2020**, *10*(5), 477, DOI: 10.3390/catal10050477.

[19] Gou, X.; Guo, Z., Hybrid Hydrophilic-Hydrophobic CuO@TiO$_2$-Coated Copper Mesh for Efficient Water Harvesting. *Langmuir.* **2020**, *36*(1), 64-73, DOI: 10.1021/acs.langmuir.9b03224.

[20] Yuan, S.; Chen, C.; Raza, A.; Song, R.; Zhang, T. – J.; Pehkonen, S. O.; Liang, B., Nanostructured TiO$_2$/CuO Dual-coated Copper Meshes with Superhydrophilic,

Underwater Superoleophobic and Self-cleaning Properties for Highly Efficient Oil/Water Separation. *Chem. Eng. J.* **2017**, *328*, 497-510. DOI: 10.1016/j.cej.2017.07.075.

[21] Ji, J.; He, H.; Chen, C.; Jiang, W.; Raza, A.; Zhang, T.-J.; Yuan, S., Biomimetic Hierarchical TiO$_2$@CuO Nanowire Arrays-Coated Copper Meshes with Superwetting and Self-Cleaning Properties for Efficient Oil/Water Separation. *ACS Sustain. Chem. Eng.* **2019**, *7*(2), 2569-2577, DOI: 10.1021/acssuschemeng.8b05570.

[22] Guo, Q.; Zhang, M.; Li, X.; Li, X.; Li, H.; Lu, Y.; Song, X.; Wang, L., A Novel CuO/TiO$_2$ Hollow Nanofiber Film for Non-enzymatic Glucose Sensing. *RSC Adv.* **2016**, *6*(102), 99969-99976, DOI: 10.1039/c6ra21628e.

[23] Tobaldi, D. M.; Espro, C.; Leonardi, S. G.; Lajaunie, L.; Seabra, M. P.; Calvino, J. J.; Marini, S.; Labrincha, J. A.; Neri, G., Photo-electrochemical Properties of CuO-TiO$_2$ Heterojunctions for Glucose Sensing. *J. Mater. Chem. A.* **2020**, *8*(28), 9529-9539, DOI: 10.1039/d0tc01975e.

[24] Dalmis, R.; Keskin, O. Y.; Ak Azem, N. F.; Birlik, I., A New One-dimensional Photonic Crystal Combination of TiO$_2$/CuO for Structural Color Applications. *Ceram. Int.* **2019**, *45*(17), 21333-21340, DOI: 10.1016/j.ceramint.2019.07.119.

[25] Stanley, J.; Sree, R. J.; Ramachandran, T.; Babu, T. G. S.; Nair, B. G., Vertically aligned TiO$_2$ Nanotube Arrays Decorated with CuO Mesoclusters for the Nonenzymatic Sensing of Glucose. *J. Nanosci. Nanotechnol.* **2017**, *17*(4), 2732-2739. DOI: 10.1166/jnn.2017.12693.

[26] Zhuravlev, M.; Sazonov, R.; Kholodnaya, G.; Pyatkov, I.; Ponomarev, D., Electrospark Method for Obtaining Nanopowders. *J. Phys. Conf. Ser.* **2019**, *1393*, 012156, DOI:10.1088/1742-6596/1393/1/012156.

[27] Remnev, G. E.; Shubin, B. G., Volume Self-Sustained Discharge in Atmospheric Pressure Gas with High Pulse Repetition Frequency. *Appl. Mech. Mater.* **2015**, *756*, 269-274.

[28] Ponomarev, D. V.; Remnev, G. E.; Sazonov, R. V.; Kholodnaya, G. E., Pulse Plasma-chemical Synthesis of Ultradispersed Powders of Titanium and Silicon Oxide. *IEEE Trans. Plasma Sci.* **2013**, *41*(10), 2908-2912,

DOI: 10.1109/TPS.2013.2273559.

[29] Remnev, G. E.; Furman, E. G.; Pushkarev, A. I.; Karpuzov, S. B.; Kondrat'ev, N. A.; Goncharov, D. V., A High-current Pulsed Accelerator with a Matching Transformer. *Instrum. Exp. Tech.* **2004**, *47*(3), 394-398, DOI: 10.1023/B:INET.0000032909.92515.b7.

[30] Hall, B. D.; Zanchet, D.; Ugarte, D., Estimating Nanoparticle Size from Diffraction Measurements. *J. Appl. Crystallogr.* **2000**, *33*(6), 1335-1341, DOI: 10.1107/S0021889800010888.

[31] Alexander, L.; Klug, H., Determination of Crystallite Size with the X-ray Spectrometer. *J. Appl. Phys.* **1950**, *21*, 137-142, DOI: 10.1063/1.1699612.

[32] Kholodnaya, G. E.; Sazonov, R. V.; Ponomarev, D. V.; Remnev, G. E.; Vikanov, A. A., Influence of Current-Conducting Inserts in a Drift Tube on Transportation of a Pulsed Electron Beam at Gigawatt Power. *Laser Part. Beams.* **2015**, *33*(4), 749-754, DOI: 10.1017/S0263034615000762.